Contact in a viscous fluid. Part 2.
A compressible fluid and an elastic solid

N. J. BALMFORTH[1,2]†, C. J. CAWTHORN[3]
AND R. V. CRASTER[4]

[1]Department of Mathematics, University of British Columbia, 1984 Mathematics Road,
Vancouver, BC V6T 1Z2, Canada

[2]Department of Earth and Ocean Science, University of British Columbia, 6339 Stores Road,
Vancouver, BC V6T 1Z4, Canada

[3]DAMTP, Centre for Mathematical Sciences, Wilberforce Road,
Cambridge CB3 0WA, UK

[4]Department of Mathematical and Statistical Sciences, University of Alberta, Edmonton,
AB T6G 2G1, Canada

A lubrication theory is presented for the effect of fluid compressibility and solid elasticity on the descent of a two-dimensional smooth object falling under gravity towards a plane wall through a viscous fluid. The final approach to contact, which takes infinite time in the absence of both effects, is determined by numerical and asymptotic methods. Compressibility can lead to contact in finite time either during inertially generated oscillations or if the viscosity decreases sufficiently quickly with increasing pressure. The approach to contact is invariably slowed by allowing the solids to deform elastically; specific results are presented for an underlying elastic wall modelled as a foundation, half-space, membrane or beam.

1. Introduction

Without additional physical effects, an object falling under gravity through an incompressible viscous fluid will take an infinite amount of time to make contact with an underlying wall if the surfaces of both are smooth and rigid. In a preceding paper (Cawthorn & Balmforth 2009), we explored how this conclusion is modified when the surfaces are not smooth but feature an asperity in the form of a sharp corner. The main focus of the complementary analysis presented here is to determine whether fluid compressibility and the elastic deformation of the solid surfaces can also modify the classical result. More specifically, we present a compressible, elasto-hydrodynamic lubrication theory for the approach of smooth surfaces to contact.

Compressible lubrication theory often features in models of gas-filled bearings (Pinkus & Sternlicht 1973), as well as in discussions of the impacts of colliding solid spheres or the coalescence of liquid droplets in gases (Hocking 1973; Barnocky & Davis 1989; Gopinath, Chen & Koch 1997). Compressibility can play a role because the large increases in pressure that occur in the fluid-filled gap between approaching surfaces can also raise local fluid densities. Perhaps equally importantly, the pressure increase can also substantially raise the fluid viscosity (the 'piezo-viscous' effect; Chu &

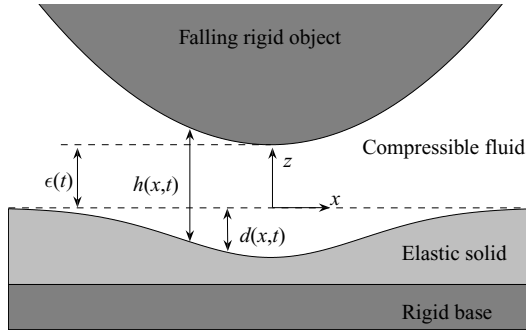† Email address for correspondence: njb@math.ubc.ca

FIGURE 1. Sketch of the sedimenting particle falling towards an elastic base.

Cameron 1962; Barus 1973). On the other hand, countering the pressure-induced rise in viscosity is the potential increase in temperature through either compression or viscous heating, which usually reduces the viscosity. In bearings and piston rings, all these effects can be important (e.g. Dowson, Ruddy & Economou 1983).

The elevated lubrication pressures also indicate that the deformability of the surfaces of the sedimenting object and wall may play a role. Elastic deformation has previously been considered for particle–particle and particle–wall collisions in viscous fluid, both theoretically (Davis, Serayssol & Hinch 1986; Barnocky & Davis 1989) and experimentally (Barnocky & Davis 1988; Verneuil *et al.* 2003). Related studies in physiology include the elasto-hydrodynamic lubrication of artificial synovial (e.g. hip) joints (Dowson & Jin 1992), cartilage biomechanics and the motion of red blood cells in blood vessels (e.g. Skotheim & Mahadevan 2005), the dynamics of cell adhesion and peeling (Weekley, Waters & Jensen 2006) and the relatively strong adhesion of the footpads of insects to vertical or inverted walls (Jiao, Gorb & Scherge 2000).

The paper is structured as follows. In §2 we formulate the problem and discuss the models that we employ for fluid compressibility and the elastic substrate. The effects of compressibility are explored in §3. Elastic substrates with the form of a foundation (mattress of springs), half-space, stretched membrane and clamped beam are considered in §4. We mention the effects of two other potentially important effects (slip and van der Waals forces) in the Appendix.

2. Formulation

The geometry of the problem is illustrated in figure 1: a two-dimensional object falls towards a nearby wall under gravity. Between the wall and the object lies a compressible fluid with velocity field $(\hat{u}, \hat{v})$, pressure $\hat{p}$, density $\hat{\rho}$ and dynamic viscosity $\hat{\mu}$. The object has a reduced mass per unit length of M in comparison with the far-field, ambient density. For simplicity, we take the object to be rigid but allow the underlying wall to deform elastically, according to some prearranged geometrical constraints; for example, as illustrated in figure 1, there could be a rigid foundation supporting a deformable layer of finite thickness. Provided the falling object is sufficiently close to the wall, the gap between the two is approximately given by

$$\hat{h} = \hat{\epsilon} + \frac{\hat{x}^2}{2L} + \hat{d}, \tag{2.1}$$

where $\hat{\epsilon}$ is the minimum separation of the undeformed surfaces, L is the local radius of curvature of the falling object, and $\hat{d}$ is the displacement of the lower surface (measured downwards).

2.1. *Fluid equations*

Invoking the lubrication approximation, the governing fluid equations are

$$\frac{\partial \hat{\rho}}{\partial \hat{t}} + \frac{\partial}{\partial \hat{x}}(\hat{u}\hat{\rho}) + \frac{\partial}{\partial \hat{z}}(\hat{w}\hat{\rho}) = 0, \tag{2.2}$$

$$\frac{\partial \hat{p}}{\partial \hat{x}} = \frac{\partial}{\partial \hat{z}}\left(\hat{\mu}\frac{\partial \hat{u}}{\partial \hat{z}}\right), \quad \frac{\partial \hat{p}}{\partial \hat{z}} = 0, \tag{2.3}$$

together with the boundary conditions

$$\hat{u} = 0 \quad \text{and} \quad \hat{w} = -\frac{\partial \hat{d}}{\partial \hat{t}}, \quad \text{on } \hat{z} = -\hat{d}, \tag{2.4}$$

$$\hat{u} = 0 \quad \text{and} \quad \hat{w} = \frac{\partial}{\partial \hat{t}}(\hat{h} - \hat{d}) \quad \text{on } \hat{z} = \hat{h} - \hat{d}. \tag{2.5}$$

At the outset, $\hat{p}(\hat{x}, 0) = \hat{p}_0$, the ambient pressure, and $\hat{\epsilon}(0) = H$, where H is the initial minimum gap thickness. Moreover, the elastic solid is initially undeformed; so $\hat{d}(\hat{x}, 0, \hat{t}) = 0$. In principle, we should further impose the far-field boundary conditions $\hat{p}(\hat{x}, \hat{t}) \rightarrow \hat{p}_0$ and $\hat{d}(\hat{x}, \hat{t}) \rightarrow 0$ as $|\hat{x}| \rightarrow \infty$. In practice, however, for the numerical computations reported later, we impose these conditions at the outer edges, $\hat{x} = \pm\hat{\ell}$, of a domain chosen large enough such that the precise length has no significant effect on the fluid dynamics (although it certainly does influence the solid mechanics as we describe later).

The equations must be supplemented by an equation of state, which, in principle, demands that we explicitly consider heat transfer and solve for the temperature field. In the interest of simplicity, we will ignore such complications and consider the barotropic law $\hat{\rho} = \hat{\rho}(\hat{p})$ with the adiabatic form $\hat{p} = K\hat{\rho}^\gamma$ taken by way of an example (with K a suitable thermodynamic constant). Also, a key feature of the problem is that the viscosity may vary, and so $\hat{\mu} = \hat{\mu}(\hat{p})$. For example, a popular model in the piezo-viscous literature is the relation of Barus (1973),

$$\hat{\mu} = \hat{\mu}_0 \exp(a\hat{p}), \tag{2.6}$$

with $\hat{\mu}_0$ a reference viscosity and a a parameter. This exponential behaviour is a fit to experimental data, and one could equally well adopt an algebraic dependence on pressure, $\hat{\mu} = \mu_0(\hat{p}/\hat{p}_0)^m$, as we shall later, to gauge the effect of pressure variations on the viscosity; the parameter m allows for viscosity increases (decreases) for $m > 0$ ($m < 0$).

2.2. *The elastic solid*

For the solid, we entertain four main options: an elastic (Winkler) foundation, a linear elastic half-space, a stretched membrane and a beam. From a theoretical perspective, the foundation is the simplest type of elastic base to explore and is typically the first model to be adopted in theoretical explorations (e.g. Skotheim & Mahadevan 2005; Weekley *et al.* 2006), even though, in principle, it applies only if the substrate is relatively thin, compressible and has an underlying rigid backing (as shown in figure 1). Though more difficult to work with, the elastic half-space is arguably more realistic. We also provide results for membranes and beams because it turns out that the detailed dynamics of the contact problem depends critically on the solid

mechanics, and so including them in our exploration gives a greater sense of the range of possibilities.

For each case, the displacement of the fluid–solid interface is related to local normal force (primarily given by the fluid pressure in lubrication theory) via the equations of linear elasticity: for the foundation,

$$\hat{p} - \hat{p}_0 = \frac{(1-v)E\hat{d}}{\delta(1+v)(1-2v)}, \tag{2.7}$$

where E is Young's modulus, v is Poisson's ratio and δ is the solid's thickness. For an elastic half space the relation between pressure and displacement is given by

$$\hat{p} - \hat{p}_0 = \frac{E}{4\pi(1-v^2)} \int_{-\infty}^{\infty} \frac{\partial \hat{d}}{\partial \hat{x}'} \frac{\mathrm{d}\hat{x}'}{(\hat{x} - \hat{x}')}, \tag{2.8}$$

as described in Muskhelishvili (1963), where the additional decoration on the integral sign signifies that the Cauchy principal value of the singular integral is taken. For the membrane,

$$\hat{p} - \hat{p}_0 = -\frac{\varpi\delta E}{(1-v^2)} \frac{\partial^2 \hat{d}}{\partial \hat{x}^2}, \tag{2.9}$$

where ϖ is the fractional change in length because of the applied tension. Finally, for the beam,

$$\hat{p} - \hat{p}_0 = \frac{E\delta^3}{12(1-v)} \frac{\partial^4 \hat{d}}{\partial \hat{x}^4}. \tag{2.10}$$

2.3. *The falling object and our main equations*

By Newton's third law, and because the pressure dominates the resistive force in lubrication theory,

$$M\frac{\mathrm{d}^2\hat{\epsilon}}{\mathrm{d}\hat{t}^2} = \int_{-\infty}^{\infty} [\hat{p}(\hat{x}, \hat{t}) - \hat{p}_0]\,\mathrm{d}\hat{x} - Mg, \tag{2.11}$$

where g is the gravitational acceleration (neglected in the equations of motion of the fluid and elastic solid). We retain the inertia of the particle whilst neglecting the fluid inertia, which is legitimate when the fluid gap is sufficiently thin. The object initially falls from rest and so $\mathrm{d}\hat{\epsilon}/\mathrm{d}\hat{t} = 0$ with $\hat{\epsilon} = H$ at $\hat{t} = 0$.

To find the lubrication pressure force that enters this equation, we integrate (2.3) to determine the velocity field and then integrate (2.2) across the gap to find the integrated mass conservation equation,

$$\frac{\partial}{\partial \hat{t}}(\hat{\rho}\hat{h}) = \frac{\partial}{\partial \hat{x}}\left(\frac{\hat{h}^3\hat{\rho}}{12\hat{\mu}}\frac{\partial \hat{p}}{\partial \hat{x}}\right). \tag{2.12}$$

Equations (2.1), (2.7)–(2.12), together with the constitutive laws, $\hat{\rho} = \hat{\rho}(\hat{p})$ and $\hat{\mu} = \hat{\mu}(\hat{p})$, comprise the main dimensional equations for our analysis.

2.4. *Non-dimensionalization*

We now rescale to remove dimensions,

$$\hat{x} = (LH)^{1/2}x, \quad (\hat{z}, \hat{h}, \hat{\epsilon}, \hat{d}) = H(z, h, \epsilon, d), \tag{2.13}$$

$$(\hat{p}, \hat{p}_0) = \frac{Mg}{\sqrt{HL}}(p, p_0), \quad \hat{t} = \frac{12\mu_0 L}{Mg}\sqrt{\frac{L}{H}}\,t, \tag{2.14}$$

to arrive at

$$\frac{\partial}{\partial t}(\rho h) = \frac{\partial}{\partial x}\left(\frac{h^3 \rho}{\mu}\frac{\partial p}{\partial x}\right), \tag{2.15}$$

$$\mathcal{M}\ddot{\epsilon} = \int_{-\infty}^{\infty} (p(x,t) - p_0)\,\mathrm{d}x - 1. \tag{2.16}$$

The fluid density and viscosity are scaled with their reference values so that the dimensionless constitutive laws are $\rho = \rho(p)$ and $\mu = \mu(p)$ (and taken as $\rho = p^{1/\gamma}$ and $\mu = p^m$ in all examples), and the parameter

$$\mathcal{M} = \frac{H^2 M^2 g}{144\mu_0^2 L^3} \tag{2.17}$$

measures the importance of the inertia of the falling object.

We write the pressure–displacement relation for the elastic lower surface formally as

$$p - p_0 = \mathcal{K} D[d], \tag{2.18}$$

where $D[d]$ is a dimensionless version of the integro-differential operators listed earlier in (2.7)–(2.10) and $\mathcal{K}$ is a dimensionless parameter measuring the strength of solid elasticity: for the elastic foundation,

$$p = p_0 + \mathcal{K}d, \quad \mathcal{K} = \frac{(1-\nu)EH\sqrt{LH}}{Mg\delta(1+\nu)(1-2\nu)}; \tag{2.19}$$

for the half-space,

$$p = p_0 + \frac{\mathcal{K}}{\pi}\int_{-\infty}^{\infty}\frac{\partial d}{\partial x'}\frac{\mathrm{d}x'}{(x-x')}, \quad \mathcal{K} = \frac{EH}{4Mg(1-\nu^2)}; \tag{2.20}$$

for the membrane,

$$p = p_0 - \mathcal{K}\frac{\partial^2 d}{\partial x^2}, \quad \mathcal{K} = \frac{\varpi\delta E\sqrt{HL}}{(1-\nu^2)MgL}; \tag{2.21}$$

and for the beam,

$$p = p_0 + \mathcal{K}\frac{\partial^4 d}{\partial x^4}, \quad \mathcal{K} = \frac{E\delta^3}{12(1-\nu)MgL\sqrt{HL}}. \tag{2.22}$$

The initial conditions are $\epsilon(0) = 1$, $\dot{\epsilon}(0) = 0$, $p(x,0) = p_0$, and we demand $p \to p_0$ and $d \to 0$ as $|x| \to \infty$ or at the edge of a finite computational domain ($x = \pm\ell$ for computations in real space; we also use a domain that shrinks in time for the computations of § 3, defined by $\xi = x/\sqrt{\epsilon(t)}$, in which case the condition is imposed at fixed $\xi = \Xi$).

To give a general idea of the parameter settings expected in a typical physical situation, consider a steel cylinder of density 8 g cm^{-3}, radius 1 cm and length 10 cm (giving a mass per unit length of $M \approx 2.5$ kg m^{-1}) falling through glycerine (density 1 g cm^{-3}) with a viscosity of 1 Pa s at near-atmospheric pressure (10^5 Pa). If the cylinder begins a distance 1 mm above the underlying wall, then $p_0 \approx 13$ and $\mathcal{M} \approx 0.43$. The elasticity parameter varies significantly according to the underlying material; considering the half-space, we estimate $\mathcal{K}$ to take values of 10^5 for a relatively hard material (such as a metal, with $E \sim 10^{10}$ Pa) or 100 for a softer material such as rubber (with $E \sim 10^7$ Pa) and even 0.1 for a very soft solid such

as gelatin ($E \sim 10^3$ Pa). Overall, it therefore seems reasonable to assume order-one values for all these parameters.

3. Compressibility

We first focus on the effect of compressibility by assuming that the lower surface is rigid, $d = 0$, implying that

$$h(x, t) = \epsilon(t) + \frac{1}{2}x^2. \tag{3.1}$$

Existing results for incompressible fluids can be recovered from (2.15) and (2.16) in the limit $p_0 \gg 1$. In that situation, at least provided that the fluid gap does not become too narrow, the pressure does not vary too much from its initial value, and we may adopt the approximations $\rho \approx 1$ and $\mu \approx 1$. The left-hand side of (2.15) then becomes $\dot{\epsilon}$, and we integrate to find the pressure distribution

$$p = p_0 - \frac{\dot{\epsilon}}{2h^2}. \tag{3.2}$$

The lubrication force is computed to be $\int (p - p_0)\,\mathrm{d}x = \pi\dot{\epsilon}/2\sqrt{2}\epsilon^{3/2}$, and the result that ϵ decreases like t^{-2} finally follows from (2.16). We emphasize this classical result here because it implies that the pressure is expected to increase continually over a range in x that shrinks with time like $x \sim \sqrt{\epsilon}$. Importantly, this motivates a convenient change of variable, $\xi = x/\sqrt{\epsilon}$, which accounts for the dynamical rescaling and expedites accurate numerical computations of the compressible problem.

With the change of variable,

$$h(x, t) = \epsilon(t)\mathscr{H}(\xi) = \epsilon(t)\left(1 + \frac{1}{2}\xi^2\right), \tag{3.3}$$

and the lubrication equations become

$$\left(\frac{\partial}{\partial t} - \frac{\dot{\epsilon}\xi}{2\epsilon}\frac{\partial}{\partial \xi}\right)[\epsilon\mathscr{H}\rho(p)] = \epsilon^2 \frac{\partial}{\partial \xi}\left[\frac{\mathscr{H}^3\rho(p)}{\mu(p)}\frac{\partial p}{\partial \xi}\right], \tag{3.4}$$

$$\mathscr{M}\ddot{\epsilon} = \sqrt{\epsilon}\int_{-\infty}^{\infty}[p(\xi, t) - p_0]\,\mathrm{d}\xi - 1. \tag{3.5}$$

We solve (3.4) and (3.5) numerically by approximating the spatial derivatives by centred finite differences on a uniform grid in ξ and then time stepping the resulting coupled ordinary differential equations using a standard stiff time integrator (MATLAB's ODE15S or the DASSL algorthm of Petzold 1983). The spatial domain is taken to be $0 \leqslant \xi \leqslant \varXi$, with suitable symmetry conditions applied at the midpoint and $\varXi$ chosen to be 20 or more, which is sufficiently large to make the precise location of the outer boundary irrelevant. A grid of 1000 points was typically used, and the integration tolerances were set to forbid errors exceeding 10^{-5}. For the elastic problems discussed later, the numerical computations are performed on a fixed, uniform grid in x, and the outer boundary conditions are applied at $x = \pm\ell$ with $\ell \geqslant 10$. As stated earlier, we take $\rho = p^{1/\gamma}$ and $\mu = p^m$.

3.1. *Numerical results*

Sample numerical solutions to (3.4) and (3.5) are shown in figure 2. Figure 2(*a*) displays the evolving pressure field on the (ξ, t)-plane for $(\mathscr{M}, p_0, \gamma, m) = (1, 2, 1, 0)$, which gradually increases in time because of the narrowing of the fluid gap, although a sequence of decaying oscillations punctuates the initial fall.
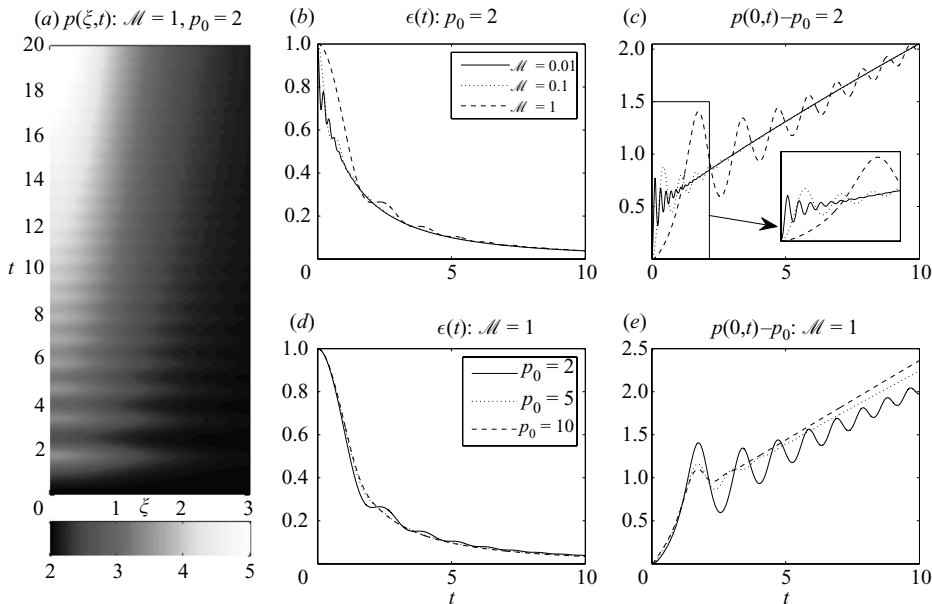
FIGURE 2. (*a*) The pressure variation versus time for $\mathcal{M} = 1$ and $p_0 = 2$; (*b*,*c*) $\epsilon(t)$ and $p(0, t) - p_0$ for $p_0 = 10$ and varying $\mathcal{M}$ with the inset in (*c*) showing the detail of the transients at small times; (*d*,*e*) $\epsilon(t)$ and $p(0, t) - p_0$ for $\mathcal{M} = 1$, with the three values of p_0 indicated. The density and viscosity laws have $m = 0$ and $\gamma = 1$.

The other panels display time series of the minimum gap thickness and central pressure $p(0, t)$, for various values of $\mathcal{M}$ and p_0, and illustrate how the initial oscillations are transients arising from the sedimenting particle's inertia: the oscillations in the time traces depend on $\mathcal{M}$ (as $\mathcal{M}$ decreases, the inertial time scale lengthens, delaying the onset of the oscillations though amplifying them), but once they decay, $\epsilon(t)$ and $p(0, t)$ converge to a common curve that is independent of both $\mathcal{M}$ and p_0. A major difference arises for the smaller values of p_0, where the inertial oscillations are persistent and even appear to grow with time. We shall return to the effects of small p_0 later.

3.2. *Long-time similarity solution*

Over long times, the numerical solutions converge to power-law behaviour in t, suggestive of a long-time similarity solution (see figure 3). The insensitivity to p_0 and $\mathcal{M}$, coupled with the equation of motion (3.5), indicate that this similarity solution must take the form

$$p = p_0 + \frac{1}{\sqrt{\epsilon}} f(\xi) \approx \frac{1}{\sqrt{\epsilon}} f(\xi), \tag{3.6}$$

with

$$\int_{-\infty}^{\infty} f(\xi) \, \mathrm{d}\xi = 1. \tag{3.7}$$

Substituting the similarity form (3.6) into (3.4) further demands that

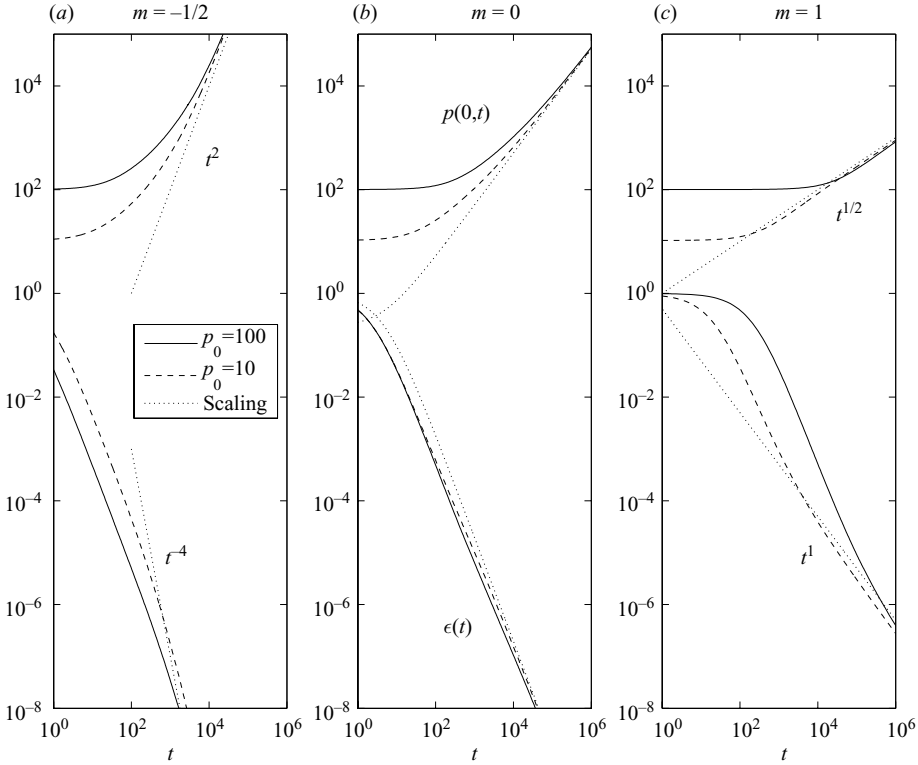$$\dot{\epsilon} = \frac{2\lambda}{m + 1} \epsilon^{(3+m)/2}, \tag{3.8}$$

FIGURE 3. The long-time scalings for $p(0,t)$ and $\epsilon(t)$ for $\mathcal{M} = 0.1$, $\gamma = 1$ and (a) $m = -1/2$, (b) $m = 0$ and (c) $m = 1$. In each case the ambient pressures $p_0 = 10$ and 100 are illustrated. In (b) the similarity solution (3.11) is the dotted line, and in the other panels the dotted line indicates the expected similarity scalings.

for some constant λ. That is

$$\epsilon \sim (1 + \lambda t)^{-2/(1+m)}, \tag{3.9}$$

using $\epsilon(0) = 1$ (which is not necessarily the correct initial condition for the final self-similar phase), reproducing the scalings evident in the numerical data. Moreover, the similarity function $f(\xi)$ satisfies

$$\frac{\lambda}{1+m} \left[(2 - \gamma^{-1}) f^{1/\gamma} \mathcal{H} - \xi (f^{1/\gamma} \mathcal{H})_\xi \right] = (\mathcal{H}^3 f^{1/\gamma - m} f_\xi)_\xi. \tag{3.10}$$

For $m = 0$ and $\gamma = 1$, (3.7), (3.8) and (3.10) have the explicit solution

$$\epsilon(t) = \frac{2\pi^2}{(\pi\sqrt{2} + t)^2}, \quad f(\xi) = \frac{1}{\pi \mathcal{H}(\xi)\sqrt{2}}. \tag{3.11}$$

For other values of m and γ, (3.10) must be solved numerically. Note that the gap thickness always decreases algebraically for the similarity solution, implying contact in infinite time. Also, the equation of state does not affect the long-time similarity scaling for $\epsilon(t)$. Thus, only the pressure dependence of the viscosity (dictated by the parameter m) affects the approach to contact, with increases in viscosity impeding contact and viscosity decreases expediting contact.
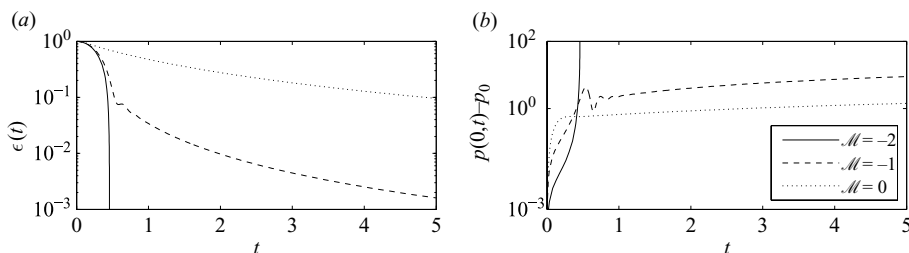
FIGURE 4. The variation of (a) $\epsilon(t)$ and (b) $p(0, t) - p_0$ for the three values of the piezo-viscosity parameter m indicated, with $\mathcal{M} = 0.1$, $p_0 = 10$ and $\gamma = 1$.

3.3. *Contact because of viscosity weakening*

The form of $\epsilon(t)$ predicted by (3.9) fails to work when $m \leqslant -1$, suggesting that a different dynamical regime exists when the viscosity decreases with pressure sufficiently quickly. Numerical computations with varying values for m that cross into this regime (and $\gamma = 1$) are shown in figure 4. The case $m = -2$ provides numerical evidence for contact in finite time.

To confirm this prediction, we retire to the case $\gamma \to \infty$, which corresponds to an incompressible fluid with a pressure-dependent viscosity. In this limit, from (2.15),

$$\dot{\epsilon} = (h^3 p^{-m} p_x)_x \longrightarrow p = \left[p_0^{1-m} - \frac{(1-m)\dot{\epsilon}}{2h^2} \right]^{1/(1-m)}. \tag{3.12}$$

Near contact, this leads to a lubrication force which, in the absence of particle inertia, implies that $\dot{\epsilon} \sim \epsilon^{(3+m)/2}$. For $m > -1$, we then recover the power-law behaviour in (3.9). If $m < -1$, on the other hand, we deduce that $\epsilon \sim (t_c - t)^{-2/(1+m)}$, with a finite contact time t_c. With $m = -1$, the approach to contact is exponential. In other words, contact occurs in finite time if the viscosity weakens sufficiently quickly with increasing pressure (with density changes playing little role).

3.4. *Contact at low ambient pressure*

The pronounced oscillations for low ambient pressures displayed in figure 2 suggest that a different dynamical regime also arises when $p_0 < 1$. A longer computation showing the oscillations for $p_0 = 1/2$, $\mathcal{M} = \gamma = 1$ and $m = 0$ is shown in figure 5 and illustrates the extremes reached as the falling object bounces above the plane. However, although $p(\xi, t)$ increases exponentially during those bounces, the quantity $A = \epsilon(t)\mathcal{H}(\xi)p(\xi, t)$ varies much less significantly. This can be understood from (3.4), which indicates that this quantity must remain roughly constant during relatively fast temporal variations provided there are no strong spatial gradients (the term $(\epsilon \mathcal{H} p)_t$ cannot be balanced in this equation if the time derivative becomes large but the ξ-derivatives remain small).

For the example shown in figure 2, the sharp bounces eventually subside, and the object approaches contact in the manner expected previously. In contrast, a computation at yet lower p_0 is shown in figure 6. In this instance, the oscillations are sufficiently severe that the falling object appears to make contact with the underlying plane after a finite number of bounces. Gopinath *et al.* (1997) have also found that contact can occur in finite time with particle inertia and fluid compressibility in the collision of spheres suspended in viscous fluid.
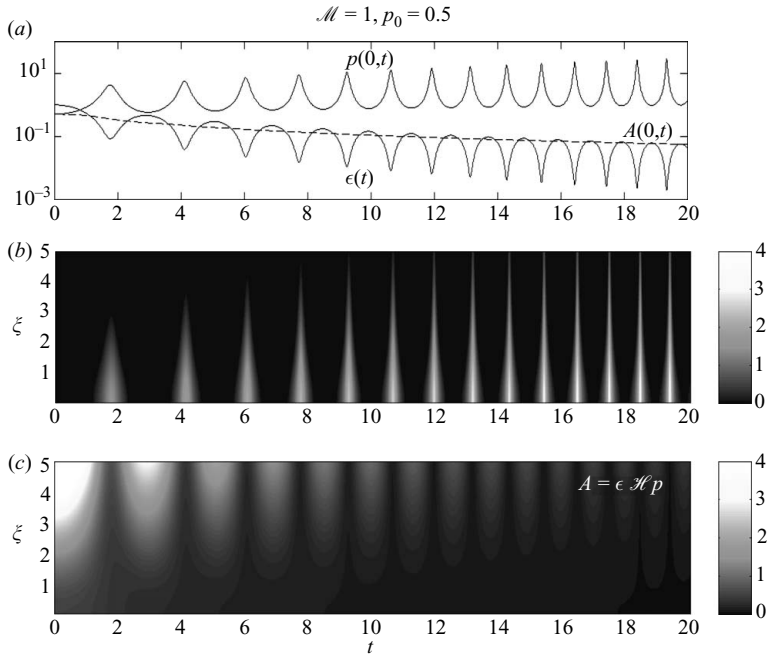
(a) $\mathcal{M} = 1, p_0 = 0.5$

FIGURE 5. A computation for $p_0 = 0.5$ and $\mathcal{M} = 1$ showing pronounced and sustained oscillations. Panel (a) shows $\epsilon(t)$, $p(0, t)$ and $A(0, t) = \epsilon \mathcal{H}(0) p(0, t)$ (dashed). Panels (b) and (c) show $\log[p(\xi, t)]$ and $A(\xi, t) = \epsilon(t) \mathcal{H}(\xi) p(\xi, t)$ as densities on the (ξ, t)-plane, respectively.
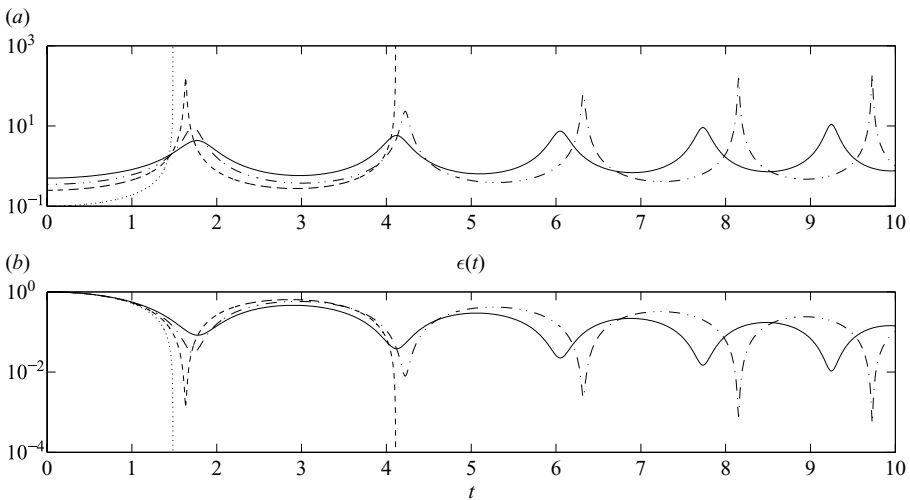

FIGURE 6. Computations at low p_0: (a) $p(0, t)$ and (b) $\epsilon(t)$ for $p_0 = 0.1$ (dotted line), $p_0 = 0.25$ (dashed line), $p_0 = 0.35$ (dot-dashed line) and $p_0 = 0.5$ (solid line).

Continuing to focus on the case $m = 0$ and $\gamma = 1$, we observe that an exact solution of (3.4) is

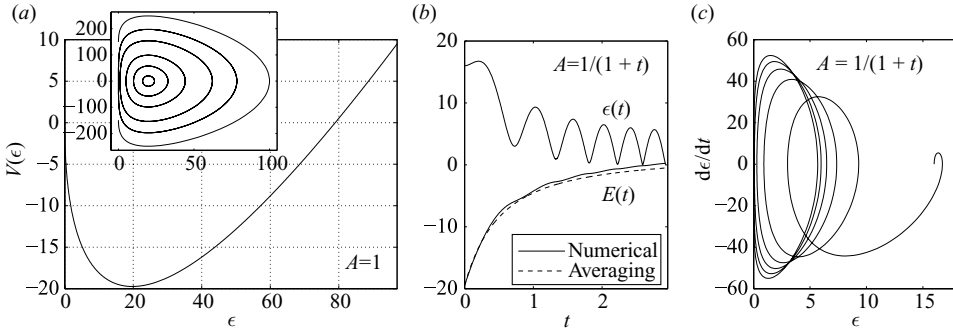$$p = \frac{A(t)}{\epsilon(t) \mathcal{H}(\xi)}, \quad \text{for} \quad A(t) = \frac{p_0}{1 + t}. \tag{3.13}$$

FIGURE 7. (a) The oscillator potential of (3.15) for $A = 1$; also plotted in the inset is a phase portrait of the solutions on the $(\epsilon, \dot{\epsilon})$-plane. The solution of the initial-value problem with $\mathcal{M} = 10^{-3}$, $\epsilon(0) = 16$, $\dot{\epsilon}(0) = 0$ and $A(t) = p_0/(1 + t)$ is shown in (b) and (c), with (b) displaying $\epsilon(t)$ and the energy $\mathscr{E}$ and (c) displaying a phase portrait on the $(\epsilon, \dot{\epsilon})$-plane.

Although this exact solution does not satisfy the correct boundary or initial conditions on $p(\xi, t)$, it does offer further insight into the compressional, inertial bounces of figure 5. Inserting the solution into (3.5), we arrive at

$$\mathcal{M}\ddot{\epsilon} = \pi A \sqrt{\frac{2}{\epsilon}} - 1, \tag{3.14}$$

which is the equation of a nonlinear oscillator with a time-dependent potential. If A were actually constant, the oscillator energy

$$\mathscr{E} = \frac{1}{2}\mathcal{M}\dot{\epsilon}^2 + V(\epsilon), \quad V(\epsilon) = \epsilon - 2\pi A\sqrt{2\epsilon}, \tag{3.15}$$

would also be constant, and the solution is given implicitly by

$$2\pi\sqrt{2}A\sin^{-1}\left(\frac{\sqrt{\epsilon} - \pi\sqrt{2}A}{\sqrt{\mathscr{E} + 2\pi^2 A}}\right) - 2\sqrt{\mathscr{E} - V(\epsilon)} = \pm\sqrt{\frac{2}{\mathcal{M}}}(t + t_0), \tag{3.16}$$

with t_0 an integration constant. The potential $V(\epsilon)$ and a phase portrait of the solutions for $A = 1$ are illustrated in figure 7. The oscillation period $4\pi^2\sqrt{\mathcal{M}}A$ is independent of the oscillator energy or equivalently the initial condition. Thus, in particular, the orbit with $\mathscr{E} = 0$ which connects the origin of the phase plane to itself traverses that trajectory in finite time.

If A is not constant but slowly varying, we can apply the method of averaging to (3.14) to determine the slow drift of the oscillator energy, an approximation that applies to the limit $\mathcal{M} \ll 1$. We substitute (3.15) into (3.14), to find $\dot{\mathscr{E}} = -2\pi\dot{A}\sqrt{\epsilon}$, and then average over the relatively fast oscillation period, holding $\mathscr{E}$ fixed and taking $\epsilon(t; \mathscr{E})$ to be given by (3.16), yielding

$$\frac{d\mathscr{E}}{dt} = -\frac{\dot{A}}{2\pi\sqrt{\mathcal{M}}A}\oint\sqrt{\epsilon}\,dt = -\frac{\dot{A}}{A}(\mathscr{E} + 6\pi^2 A^2). \tag{3.17}$$

Hence,

$$\mathscr{E} = \frac{1}{A}[\mathscr{E}(0) + 2\pi^2] - 2\pi^2 A^2. \tag{3.18}$$

A sample numerical solution of (3.14) with $\mathcal{M} = 10^{-3}$, $\epsilon(0) = 16$ and $A(t) = 1/(1 + t)$ (which is designed to compare with the averaging result and does not correspond
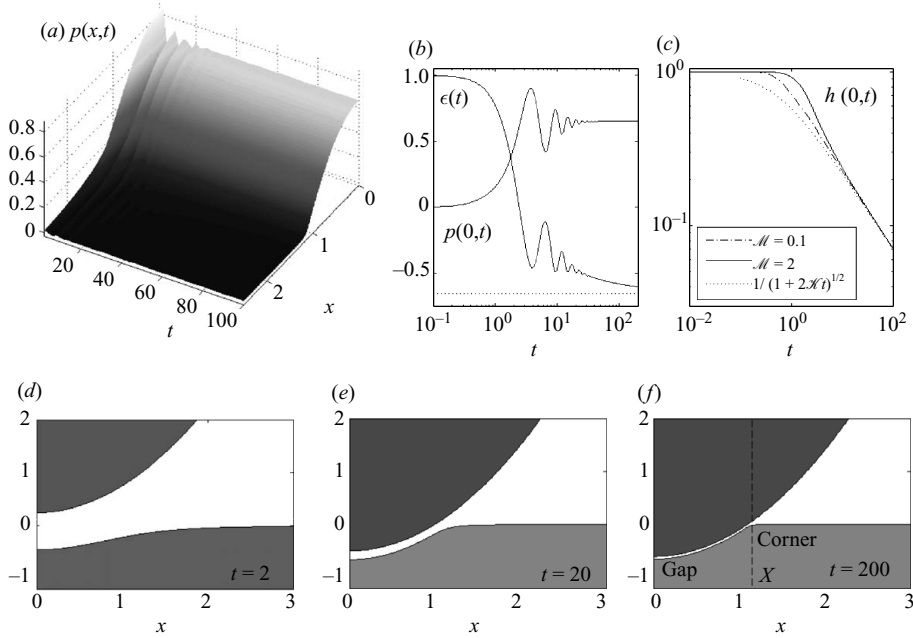
FIGURE 8. Solution for the elastic foundation with $\mathcal{M} = 2$, $\mathcal{K} = 1$ and $\ell = 10$. Shown are (a) the pressure distribution $p(x, t)$ as a surface above the (t, x)-plane, (b) $\epsilon(t)$ and $p(0, t)$ and (c) the central gap thickness $h(0, t)$. The dotted line in (b) shows the asymptote from (4.4); (c) includes data from a second computation with the lower mass, $\mathcal{M} = 0.1$, and the long-time asymptote, $h(0, t) \sim (1 + 2\mathcal{K} t)^{-1/2}$. Three snapshots of the fluid gap are shown in (d–f) at the times indicated.

to our original problem) is shown in figure 7; the oscillator energy increases monotonically in time. Thus, states that fall initially into the potential well with $\mathcal{E}(0) < 0$ execute transient oscillations before eventually gaining positive energy and intersecting $\epsilon = 0$ after a finite time.

4. Elastic deformation

Given that high pressures can arise beneath the sedimenting object, it is natural that the substrate could respond by deforming elastically. We consider elastic deformation without fluid compressibility and return to (2.15) with $\rho = \mu = 1$:

$$\frac{\partial h}{\partial t} = \dot{\epsilon} + \frac{\partial d}{\partial t} = \frac{\partial}{\partial x} \left(h^3 \frac{\partial p}{\partial x} \right), \qquad (4.1)$$

with $p - p_0 = \mathcal{K} D[d]$, $p(x, 0) = p_0$ and $d(x, 0) = 0$. Once more we solve the equations numerically in conjunction with (2.16), using a scheme similar to the compressible problem but imposing the boundary conditions $p \to p_0$ and $d \to 0$ at $x = \ell$. The parameter p_0 now becomes irrelevant, with pressure differences from the ambient playing the only role; consequently we lighten the mathematical formulae below by setting $p_0 = 0$.

4.1. The elastic foundation

A numerical solution for the elastic foundation ($p = \mathcal{K} d$) is displayed in figure 8. The object falls from its initial position, raising the fluid pressure directly underneath
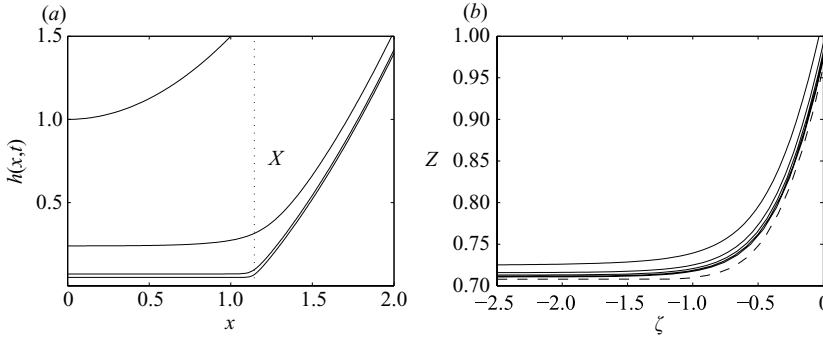
FIGURE 9. The behaviour near $x = X = (3/2\mathcal{K})^{1/3}$, for $\mathcal{M} = 2$, $\mathcal{K} = 1$: (*a*) the emergence of a sharp corner near $x = X$ in snapshots of $h(x, t)$ for $t = 2, 10, 100$ and 200; (*b*) illustrates the collapse of the height profiles (at the times $t = 20$ up to $t = 200$ in steps of 20) under the scalings $\zeta = t^{1/2}(x - X)$ and $h = Z(\zeta)t^{-1/2}$ and limit to an asymptotic solution denoted by the dashed line (satisfying $[Z^3(X - Z_\zeta)]_\zeta = 0$, with $Z_\zeta \to X$ as $\zeta \to \infty$ and $Z \to 1/\sqrt{2\mathcal{K}}$ as $\zeta \to -\infty$; Weekley *et al.* 2006).

(figure 8*b*), which correspondingly depresses the surface of the elastic solid (figure 8*d*). The descent of the object is interrupted by a series of inertial, decaying oscillations. Those bounces eventually disappear to leave a quasi-steady state in which the object sits close to its rest position, wherein the weight is balanced by the elastic forces. A finite, but gradually thinning, fluid gap still persists, however, with the fluid pressure field transmitting the upward elastic forces on to the object. The gap appears to thin at the rate $t^{-1/2}$, substantially slower than for a rigid surface. The thin gap is connected to the exterior fluid via gradually narrowing 'corner regions' (figure 9).

To understand the long-time dynamics illustrated in figure 8, we pass to the limit in which $h \ll 1$, implying

$$h \equiv \epsilon + \frac{1}{2}x^2 + d = \epsilon + \frac{1}{2}x^2 + \mathcal{K}^{-1}p \approx 0 \longrightarrow p \approx -\mathcal{K}\left(\epsilon + \frac{1}{2}x^2\right). \quad (4.2)$$

Since the object has largely ended its fall, (2.16) becomes

$$1 \approx \int_{-\infty}^{\infty} p \, \mathrm{d}x \to \int_{-X}^{X} p \, \mathrm{d}x \approx -2\mathcal{K}\left(\epsilon + \tfrac{1}{6}X^2\right) X, \quad (4.3)$$

where $(-X, X)$ is the horizontal length of the gap (the depressed section of the elastic foundation). Equation (4.3) expresses the force balance between the weight of the fallen object and the upward elastic reaction, as transmitted by the fluid pressure. Moreover, because $d \approx -(\epsilon + \tfrac{1}{2}x^2) \to 0$ at the corner (see figure 8), $\epsilon + \tfrac{1}{2}X^2 \approx 0$ and

$$X \approx \left(\frac{3}{2\mathcal{K}}\right)^{1/3} \quad \text{or} \quad \epsilon \approx -\frac{1}{2}\left(\frac{3}{2\mathcal{K}}\right)^{2/3}. \quad (4.4)$$

Returning now to (4.1),

$$\frac{\partial h}{\partial t} \approx -\mathcal{K}\frac{\partial}{\partial x}(xh^3), \quad (4.5)$$

which is solved by the method of characteristics to give the implicit solution,

$$h = (1 - 2\mathcal{K}th^2)^{1/2}h_0[x^{3/2}(1 - 2\mathcal{K}th^2)^{3/2}], \quad (4.6)$$

where $h_0(x)$ is a suitable initial condition that should, in principle, be matched to the full numerical solution at the beginning of the quasi-steady phase of evolution. Irrespective of that initial condition, underneath the centre of the falling object, we find

$$h(0, t) = \frac{h_0(0)}{\sqrt{1 + 2\mathcal{K} t h_0(0)^2}}, \tag{4.7}$$

which recovers the $t^{-1/2}$ thinning of the gap. A similar result was derived previously by Weekley *et al.* (2006), together with an asymptotic self-similar solution for h, which also holds in the present context (see figure 9).

The physical interpretation of these results is that as the falling object approaches its final position, fluid is driven out of the residual gap by the gradient of the pressure field that is set up by the elastic solid to balance the object's weight. The pressure field is determined purely by the mechanics of the elastic solid in what is equivalent to a classical type of punch problem. This interpretation is not obviously specific to the elastic foundation and, in principle, applies to any underlying elastic solid. Indeed, in all the examples we consider, inertial transient bounces precede a much slower phase in which the object lies close to its final position, and a squeeze flow clears out residual fluid from an intervening gap. Moreover, that gap invariably contains a central core with elevated pressures dictated by the elastic solid and is connected by narrowing corner zones to an outer region at the ambient pressure. Such 'dimple dynamics' bears similarities with that observed in studies of impacting viscous drops (Gopinath & Koch 2002; Griggs, Zinchenko & Davis 2008).

Nonetheless, differences between the various cases do arise because the limiting pressure field depends sensitively on the mechanics of the elastic solid, which impacts the clearing of the residual gap. Consequently, the approach to contact depends upon the precise elastic model, as illustrated by the next three examples. This also suggests that the dynamics will be different still if the falling object is made elastic (except if that object has a rigid core with an elastic coating, which leads to an identical problem to our elastic foundation).

4.2. *An elastic half-space*

For the elastic half-space, the pressure and deformation are related via the non-local relation (2.20). A sample numerical solution is shown in figure 10. As mentioned above, although the sedimentation dynamics are qualitatively similar to that seen for the foundation, the approach to contact is quantitatively different: the gap thins most rapidly over the corner regions, which close like $t^{-9/16}$ and trap a gradually decreasing amount of fluid underneath the object (so that the central core of the gap closes like $t^{-1/2}$).

As also emphasized earlier, the explanation for this behaviour lies in the limiting pressure distribution, which is equivalent to the classical solution for the indentation of a frictionless parabolic punch into a half-space (Muskhelishvili 1963): for $|x| < X$, where the object is almost in contact with the underlying solid,

$$d = -\epsilon - \frac{1}{2} x^2 \quad \text{and} \quad p = \mathcal{K} \sqrt{X^2 - x^2}. \tag{4.8}$$

Beyond, in $|x| > X$, $p \to 0$ and

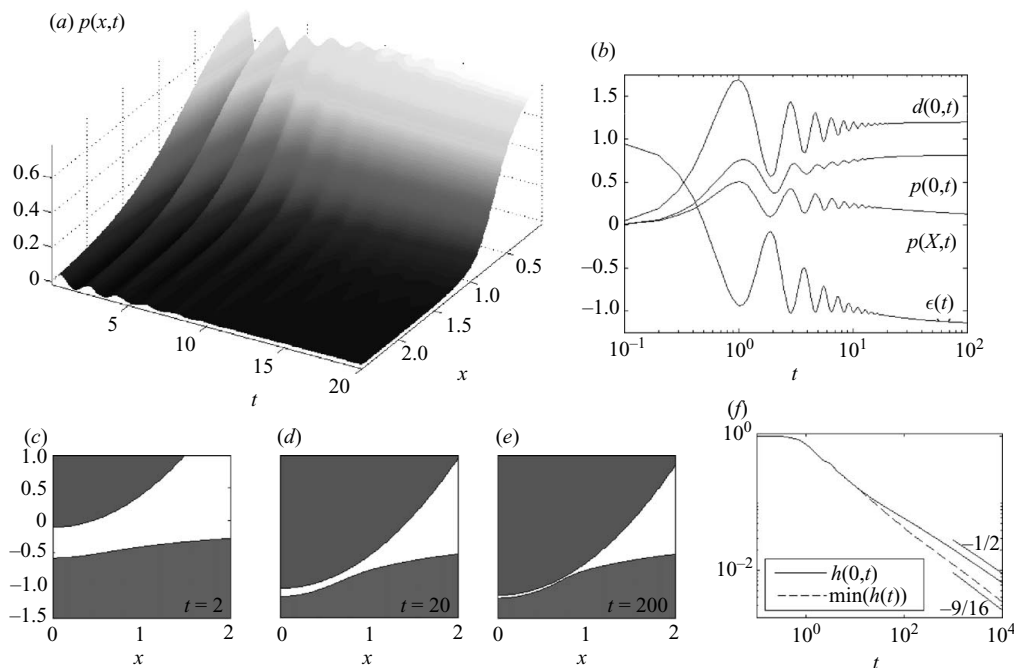$$\frac{\partial d}{\partial x} = \sqrt{x^2 - X^2} \, \text{sgn}(x) - x \tag{4.9}$$

FIGURE 10. Solution for the elastic half-space with $\mathcal{M} = 0.1$, $\mathcal{K} = 1$ and $\ell = 10$: (*a*) displays the pressure distribution $p(x, t)$ as a surface above the (t, x)-plane; shown in (*b*) are $\epsilon(t)$, $p(0, t)$, $p(X, t)$ and $d(0, t)$; (*c–e*) show snapshots of the fluid gap at the times indicated; (*f*) shows the gap thickness at the centre, $h(0, t)$, and at the corner $h(X, t)$, together with the expected limiting scalings.

or

$$d = \frac{1}{2}\left[|x|\sqrt{x^2 - X^2} - \ell\sqrt{\ell^2 - X^2} - x^2 + \ell^2 - X^2 \cosh^{-1}\left(\frac{x}{X}\right) + X^2 \cosh^{-1}\left(\frac{\ell}{X}\right) \right].$$

(4.10)

Force balance ($\int p\,\mathrm{d}x = 1$) and the continuity of d at $x = \pm X$ then imply that

$$X = \sqrt{\frac{2}{\pi}} \quad \text{and} \quad \epsilon = -\frac{1}{2}\left[\ell^2 - \ell\sqrt{\ell^2 - X^2} + X^2 \cosh^{-1}\left(\frac{\ell}{X}\right) \right].$$

(4.11)

Note that the displacement field (4.10) grows logarithmically at large x, a standard feature in planar elasticity; because we impose $d \to 0$ at the edge of our computational domain, $x = \ell$, this introduces a weak dependence of the solution on ℓ. The gradient of the pressure distribution in (4.8), which expels fluid from the gap, also diverges at $x = \pm X$. Although the divergence is actually prevented by the flow dynamics in the vicinity of the corners during the approach to contact, the gap nevertheless closes quickest there.

The scalings characterizing the approach to contact can be confirmed by matched asymptotic analysis, the details of which are sketched as follows: for the central core of the gap, substitution of the pressure solution into (4.1) furnishes

$$h_t \approx -\mathcal{K}\frac{\partial}{\partial x}\left(\frac{h^3 x}{\sqrt{X^2 - x^2}} \right),$$
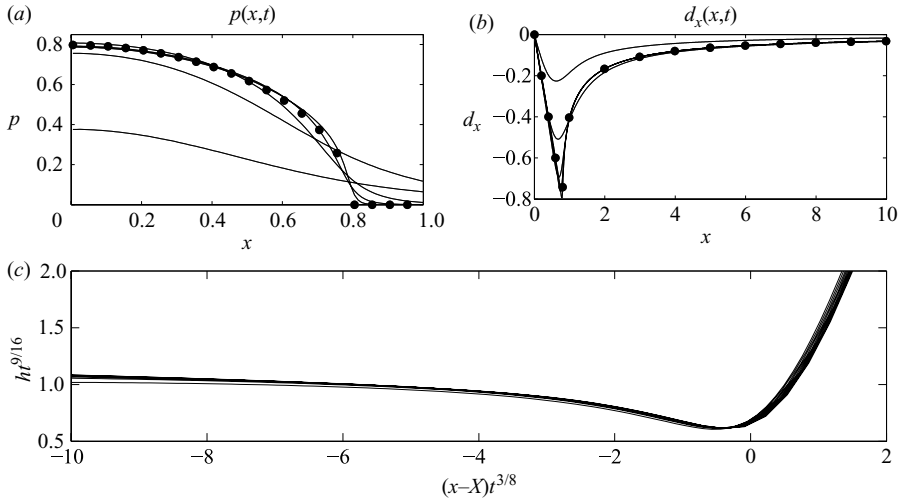
(4.12)

FIGURE 11. The (*a*) pressure and (*b*) displacement gradients for $t = 1, 10, 10^2, 10^3, 10^4$, illustrating the convergence of the numerical solutions to the asymptotic long-time behaviour (shown by the dots, as given by (4.8) and (4.9)); (*c*) shows the collapse of the data under the asymptotic scalings suitable for the corner, for $t = 10^3$ to $t = 10^4$ in steps of 10^3.

which may again be solved by the method of characteristics (cf. (4.5)). Alternatively, we can find a separable solution, $h(x, t) = t^{-1/2} G(x)$, describing the eventual closure. Importantly, we discover that $G(x) \sim (X - |x|)^{1/6} + \dots$, as $x \to \pm X$ from within the gap. Conversely, given (4.9) or (4.10), it follows that $h(x, t) \sim (|x| - X)^{3/2}$, as $x \to \pm X$ from outside the gap. Over the corner regions surrounding $|x| = X$, one can find a similarity solution $h(x, t) = t^{-\beta} J(\zeta)$ in terms of a stretched variable $\zeta = (|x| - X) t^s$. Demanding that this solution matches with the limits of the adjoining 'outer' solutions to either side of the corner determines the exponents $\beta = 9/16$ and $s = 3/8$. The convergence of a numerical solution to the form expected from the preceding arguments is illustrated in figure 11.

4.3. *The membrane*

A sample numerical solution for the stretched membrane (with $p = -\mathcal{K} d_{xx}$) is shown in figure 12. The transient inertial oscillations are now relatively pronounced but again give way to leave a quasi-steady, thinning gap. The approach to contact is slower than for the foundation and half-space, with the central core of the gap thinning like $t^{-1/4}$ and the corners closing with $t^{-1/2}$.

The relatively slow approach to contact is straightforward to rationalize in terms of the limiting pressure distribution: putting $h \ll 1$ over the core of the gap, $|x| < X$, and setting p at the ambient level beyond, $|x| > X$, we find

$$d \approx \begin{cases} -\epsilon - \dfrac{1}{2} x^2, & |x| < X, \\ X(\ell - |x|), & X < |x| \end{cases} \quad \text{and} \quad p \approx \begin{cases} \mathcal{K}, & |x| < X, \\ 0, & X < |x|, \end{cases} \tag{4.13}$$

with

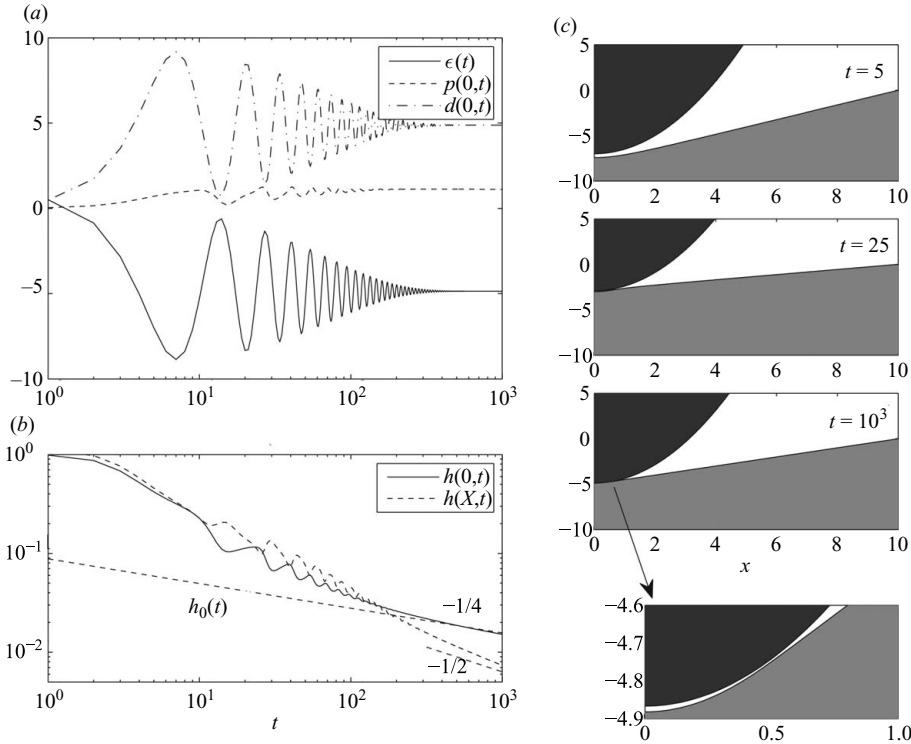$$X = \frac{1}{2\mathcal{K}} \quad \text{and} \quad \epsilon = -X \left(\ell - \frac{1}{2} X \right) \tag{4.14}$$

FIGURE 12. Solution for the membrane with $\mathcal{M} = 1$, $\mathcal{K} = 1$ and $\ell = 10$. Shown in (*a*) are $\epsilon(t)$, $p(0, t)$ and $d(0, t)$; (*b*) shows the gap thickness at the centre, $h(0, t)$, and at $X = 1/2\mathcal{K}$, $h(X, t)$, together with the predicted scalings and $h_0(t)$ from (4.16). The right-hand column of the panels marked as (*c*) show snapshots of the fluid gap at the times indicated, with the final picture showing a magnification of the closing gap in the snapshot at $t = 10^3$.

demanded by the force balance and continuity of d. Thus, the pressure gradient driving the fluid out of the gap is much reduced (and vanishes to leading order). The gradients remain largest over the corner regions, which become bottlenecks for the flow.

The long-time behaviour is rationalized by adapting asymptotic analysis presented by Jones & Wilson (1978): inside the central core of the gap, we discard the time derivative in (4.1), integrate in x and apply a no-flux condition at $x = 0$, to find $h_{xxx} \sim 0$. Because $h \to 0$ at $x = \pm X$ and $h_x(0, t) = 0$, this provides the leading-order gap thickness $h(x, t) \sim (1 - x^2/X^2)h_0(t)$ with $h_0(t)$ to be determined by matching with the solution over the corner regions. Beyond the gap, on the other hand, we have the steady state profile, $h(x, t) \to (|x| - X)^2/2$. For the corner regions, a similarity solution can be found:

$$h(x, t) = h_0^2(t)J(\zeta), \quad \zeta = \frac{|x| - X}{h_0(t)}, \tag{4.15}$$

with

$$h_0(t) = \left(1 + \frac{6\mathcal{K}\Lambda t}{X}\right)^{-1/4} \quad \text{and} \quad J_{\zeta\zeta\zeta} = \frac{\Lambda}{J^3}. \tag{4.16}$$

The constant Λ, which approximately equals 1385 for the example in figures 12 and 13, is found by integrating the differential equation for J numerically, imposing boundary
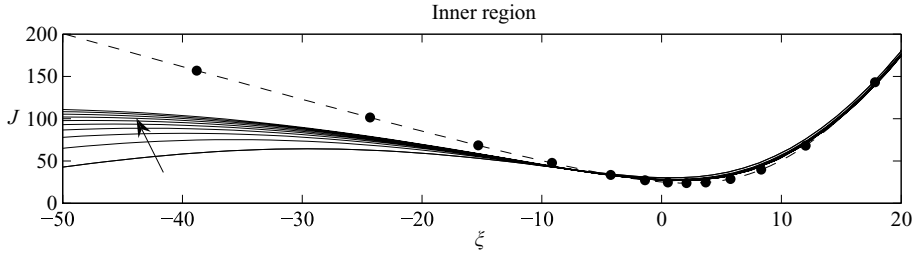
FIGURE 13. The corner region at $x = X$ showing the collapse of the height field (the solid lines at $t = 1000, 2000, \ldots, 10\,000$) to the similarity solution (circles and dashed line) $J(\zeta)$.

conditions demanded by matching: $(J, J', J'') \to (-2\zeta/X, -2/X, 0)$ as $\zeta \to -\infty$ and $J'' \sim 1$ as $\zeta \to \infty$ (cf. Jones & Wilson 1978). By way of comparison with the preceding results, figures 12(b) and 13 show, respectively, the evolution of the central and corner gap thicknesses in time and the collapse of snapshots of $h(x,t)$ under the similarity scaling in (4.15).

4.4. The beam

For the beam, $p = \mathcal{K} d_{xxxx}$, and we must supply additional boundary conditions at the edges of the domain; we adopt clamped conditions with $d(\pm\ell, t) = d_x(\pm\ell, t) = 0$. A sample numerical solution is shown in figure 14; although transient oscillations once more punctuate the initial fall and subside to leave a quasi-static settling phase, the final evolution now shows an qualitative difference with the previous examples – instead of fluid being gradually squeezed out of a thinning gap, a central, static bubble now emerges with constant pressure that supports the weight of the object. The fluid thins to contact only at the corners, $x = \pm X$, and the fluid in the bubble becomes permanently pressurized and trapped beneath the object.

The limiting state is given by

$$
p = \begin{cases} P, & |x| < X, \\ 0, & X < |x|, \end{cases} \quad \text{and} \quad h \equiv h_{eq}(x) = \frac{1}{12\mathcal{K}} \begin{cases} |x|(|x| - X)^2, & |x| > X, \\ \frac{1}{2}P(x^2 - X^2)^2, & |x| < X, \end{cases} \tag{4.17}
$$

where P is the excess bubble pressure and

$$
P = \frac{1}{2X}, \quad X = 2\ell - \sqrt{\ell(\ell + 12\mathcal{K})} \quad \text{and} \quad \epsilon = \frac{1}{12\mathcal{K}}\ell(\ell - X)^2 - \frac{1}{2}\ell^2, \tag{4.18}
$$

given the requirements of force balance and the continuity of d and its first three derivatives. Thus, once again, the pressure in the gap is unable to effectively drive out the intervening fluid; coupled with the stiffness of the underlying beam, this generates the permanent bubble.

The approach to the final state observed numerically is rationalized as follows: we first set $h - h_{eq} = \theta(x, t)$ for the residual gap thickness. Everywhere but in the vicinity of the corners, $h_{eq} \gg \theta \sim O(\Delta)$, where $\Delta(t) \ll 1$ is the time-dependent magnitude of the residual. Near the corners, however, θ and $h_{eq} \approx (X - |x|)^2 X/12\mathcal{K}$ must be comparable, implying a characteristic length scale of $|x| - X \sim O(\Delta^{1/2})$. In turn, from the beam equation, this indicates that the residual gap thickness must be constant in space to leading order: $\theta = \Delta(t)$ (over the corner regions, $p = O(1)$, but $\mathcal{K} d_{xxxx} \to \mathcal{K}\theta_{xxxx} \sim O(\Delta^{-1})$; moreover, outside those regions, $\theta_{xxxx} \sim 0$, and so
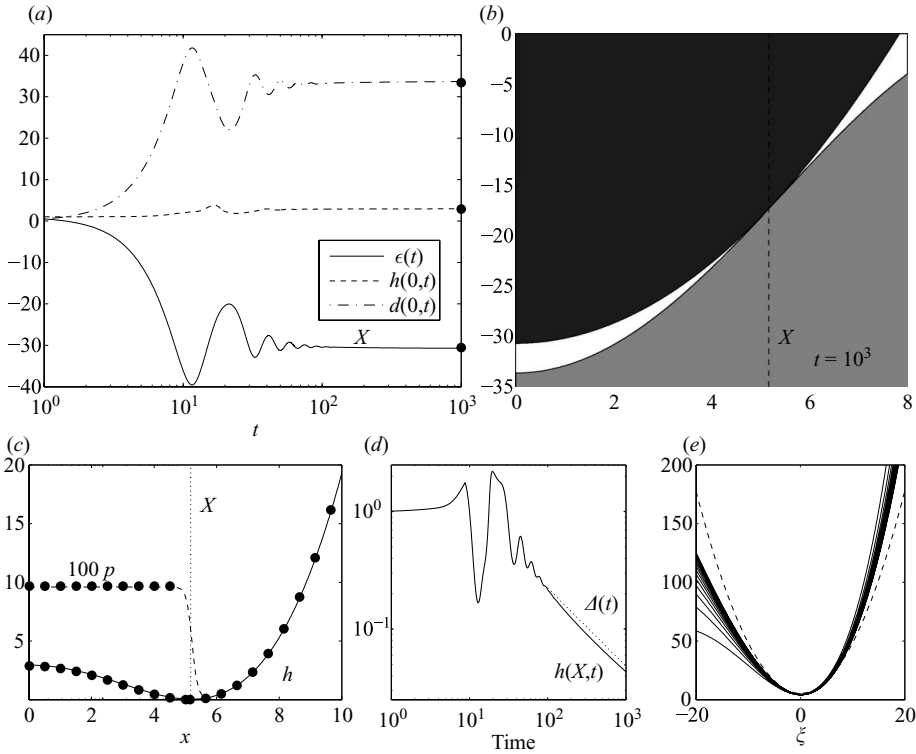
FIGURE 14. A numerical solution for the beam with $\mathcal{M} = \mathcal{K} = 1$ and $\ell = 10$. In (*a*) are shown $\epsilon(t)$, $h(0,t)$ and $d(0,t)$; the dots indicate the expected long-time results; (*b*) shows h and $\epsilon + x^2/2$ at $t = 10^3$; (*c*) shows h and p (scaled by a factor of 100) at the same instant, with the dots indicating the expected final values; (*d*) shows the gap thickness at the corner, $h(X,t)$, together with $\Delta(t)$ from (4.22); (*e*) shows the collapse of snapshots of the height field (at $t = 100, 200, \ldots, 1000$) using the self-similar variables, $t^{2/3}h(x,t)$ and $t^{1/3}(x - X)$; the dashed line denotes prediction in (4.20).

a match of the solutions, together with the boundary conditions at $x = 0$ and ℓ, demands the result).

Given these scalings (and their implication that $|(h^3 p_x)_x| \gg |h_t|$ near the corners), we now equate the flux through each corner region, $h^3 p_x$, with the rate of leakage of the residual extra fluid from half of the bubble, $X\dot{\Delta}$, giving

$$p_x \approx \pm \frac{X\dot{\Delta}}{h^3}, \tag{4.19}$$

where

$$h \approx \frac{X}{12\mathcal{K}}(|x| - X)^2 + \Delta. \tag{4.20}$$

The integral of the left-hand side of (4.19) must furnish the pressure jumps across each corner region. Considering explicitly the jump of $-P$ across the corner at $x = X$,

$$-P \approx X\dot{\Delta} \int_{-\infty}^{\infty} \frac{\mathrm{d}(x - X)}{[X(x - X)^2/12\mathcal{K} + \Delta]^3} = \frac{3\pi}{8} X\Delta^{-5/2}\dot{\Delta}\sqrt{\frac{12\mathcal{K}}{X}}. \tag{4.21}$$

	$h(0, t) \sim t^{-b}$	$h(X, t) \sim t^{-\beta}$
Foundation	$b = 1/2$	$\beta = 1/2$
Half-space	1/2	9/16
Membrane	1/2	1/4
Beam	0	2/3

TABLE 1. A summary of the long-time asymptotic scaling of the central and corner gap thicknesses.

Thus,

$$\Delta \approx \left(\frac{\pi}{4P} \sqrt{\frac{12\mathscr{K}}{X}} \right)^{2/3} t^{-2/3}. \tag{4.22}$$

In figure 14, the prediction for $\Delta(t)$ is compared with the numerical result for the gap thickness at the corner, $h(X, t)$. Figure 14(e) also shows how scaled snapshots of numerical solutions, $t^{2/3}h(x, t)$ versus $t^{1/3}(x - X)$, collapse towards a common curve in line with the predictions in (4.20) and (4.22).

In summary, the approach to contact reflects the pressure distribution set by the elastic deformation required to accommodate the gravitational force exerted by the sedimented object. For the foundation, the entire gap controls the limiting flow dynamics, but for the half-space the corner plays the main role because the limiting pressure gradient diverges there. The approach to contact is different still for the stretched membrane and beam; table 1 summarizes the various results. The membrane and beam behave quite differently primarily because the pressure in the core of the gap becomes constant in space. This is ineffective at expelling the intervening fluid and leads to bottlenecks in the flow over the corner regions. As a consequence, the approach to contact for the membrane becomes the slowest of all four examples, whereas the beam traps a permanent pressurized fluid bubble underneath the fallen object.

5. Discussion

The current paper has explored how fluid compressibility and solid elasticity affect the approach to contact of a two-dimensional object sedimenting through a viscous fluid towards a plane wall; without either effect, contact takes an infinite time. Fluid compressibility allows contact to occur in finite time via two possible pathways. First, if the viscosity decreases sufficiently rapidly with increasing pressure, the lubrication force is unable to diverge rapidly enough to halt the descent of the object. Second, the object's inertia triggers a series of oscillations or bounces during the initial fall; if ambient pressures are low enough, the oscillations become sufficiently severe to force an impact at the minimum of the bounce. Allowing the surfaces to deform elastically slows the approach to contact to a degree that depends sensitively on the solid mechanics; we have presented four examples (a foundation, half-space, membrane and beam) to illustrate the range of possibilities. The crucial detail is the limiting pressure distribution set up by the elastic solid to balance the weight of the fallen object, because its gradient is responsible for expelling the intervening fluid. In the Appendix, we also mention the effects of wall slip and van der Waals forces, which provide alternative routes to contact in finite time for situations in which the gap closes sufficiently to demand the introduction of molecular effects (cf. Hocking 1973;

Serayssol & Davis 1986; Gopinath *et al.* 1997). All in all, the pathway to achieving contact is strewn with competing physical effects, and in any given situation careful attention must be paid to those that dominate.

A major simplification in the present work has been our restriction to two spatial dimensions. Nevertheless, much of the analysis we have presented for the approach to contact can be adapted to the problem of a sphere falling onto a plane. This indicates that many of the conclusions and long-time scalings also apply in three-dimensional, axisymmetrical situations. Despite this, an interesting extension of the current work would be to allow flow perturbations to break the axial symmetry (axisymmetry) in the cylindrical (spherical) version of the problem: our results suggest that bottlenecks often develop as approaching elastic surfaces try to drive fluid out of the intervening gap. Should fluid be able to migrate asymmetrically within these bottlenecks to bypass them, three-dimensional instabilities may arise, as in the Saffman–Taylor problem (Saffman & Taylor 1958), the printer's instability (Pearson 1960) and the fingering of contact lines and surfactant-driven droplets (Huppert 1982; Warner, Craster & Matar 2004).

Appendix. Slip and van der Waals

Consider a constant-viscosity, incompressible fluid sandwiched between rigid smooth surfaces (cf. Hocking 1973). Near contact, the lubrication analysis predicts the velocity field,

$$u = -6(p + \alpha h^{-3})_x z(h - z) + \left(1 - \frac{z}{h}\right) u_0 + \frac{z}{h} u_h, \tag{A 1}$$

which incorporates the van der Waals disjoining pressure with a Hamaker constant α and where u_0 and u_h are the slip velocities on $z = 0$ and $z = h$, respectively. We use the Navier slip conditions, $u_z(z = 0) = Su_0$ and $u_z(z = h) = -Su_h$, where S is the inverse of a characteristic slip length, which indicate that

$$Su_0 = Su_h = -6h(p + \alpha h^{-3})_x. \tag{A 2}$$

The vertically integrated mass conservation equation (2.15) now yields

$$\dot{\epsilon} = \left[\left(h + \frac{6}{S}\right) h^2 (p + \alpha h^{-3})_x\right]_x, \tag{A 3}$$

which is integrated in x to provide the pressure field,

$$p = p_0 - \frac{\alpha}{h^3} + \frac{1}{36} S^2 \dot{\epsilon} \left[\log\left(1 + \frac{6}{Sh}\right) - \frac{6}{Sh}\right]. \tag{A 4}$$

The equation of motion of the falling object now follows:

$$\mathscr{M}\ddot{\epsilon} = -1 - \frac{3\pi\alpha\sqrt{2}}{8\epsilon^{5/2}} - \frac{\pi S^2}{18} \dot{\epsilon}\sqrt{2} \left[\frac{3}{S}\epsilon^{-1/2} + \epsilon^{1/2} - \left(\epsilon + \frac{6}{S}\right)^{1/2}\right]. \tag{A 5}$$

Without slip ($S \to \infty$), the van der Waals forces and the resistive lubrication force eventually dominate the gravitational force and inertia, and the approach to contact

becomes dictated by $2\epsilon\dot{\epsilon} \sim -3\alpha$. Contact therefore occurs at the finite time $t = t_c$, with $\epsilon \sim \sqrt{3\alpha(t_c - t)}$.

Without van der Waals forces ($\alpha = 0$), and in the limit $\epsilon \to 0$,

$$\mathscr{M}\ddot{\epsilon} \sim -1 - \tfrac{1}{6}\pi S\dot{\epsilon}\sqrt{2}\epsilon^{-1/2}. \tag{A 6}$$

When inertia is negligible, $\mathscr{M} \ll 1$, there is contact in finite time with $\epsilon \sim (1/2)[3(t_c - t)/\pi S]^2$. Inertia leaves this time dependence unaltered for $S^2/\mathscr{M} > 36/\pi^2$ with $\epsilon \sim \beta^2(t_c - t)^2$ and β determined from $6\mathscr{M}\beta^2 - \sqrt{2\pi S}\beta + 3 = 0$. Otherwise, one observes contact in finite time with $\epsilon \propto (t_c - t)$.

REFERENCES

BARNOCKY, G. & DAVIS, R. H. 1988 Elastohydrodynamic collision and rebound of spheres: experimental verification. *Phys. Fluids* **31**, 1324–1329.

BARNOCKY, G. & DAVIS, R. H. 1989 The influence of pressure-dependent density and viscosity on the elastohydrodynamic collision and rebound of two spheres. *J. Fluid Mech.* **209**, 501–519.

BARUS, H. 1973 Inlet shear heating in elastohydrodynamic lubrication. *ASME J. Lubr. Technol.* **95**, 417–426.

CAWTHORN, C. J. & BALMFORTH, N. J. 2010 Contact in a viscous fluid. Part 1. A falling wedge. *J. Fluid Mech.* **646**, 327–338.

CHU, P. S. Y. & CAMERON, A. 1962 Pressure viscosity characteristics of lubricating oils. *J. Inst. Petrol.* **48**, 147–155.

DAVIS, R. H., SERAYSSOL, J.-M. & HINCH, E. J. 1986 The elastohydrodynamic collision of two spheres. *J. Fluid Mech.* **163**, 479–497.

DOWSON, D. & JIN, Z. M. 1992 Microelastohydrodynamic lubrication of low-elastic-modulus solids on rigid substrates. *J. Phys* D **25**, A116–A123.

DOWSON, D., RUDDY, B. L. & ECONOMOU, P. N. 1983 The elastohydrodynamic lubrication of piston rings. *Proc. R. Soc. Lond.* A **386**, 409–430.

GOPINATH, A., CHEN, S. B. & KOCH, D. L. 1997 Lubrication flows between spherical particles colliding in a compressible non-continuum gas. *J. Fluid Mech.* **344**, 245–269.

GOPINATH, A. & KOCH, D. L. 2002 Collision and rebound of small droplets in an incompressible continuum gas. *J. Fluid Mech.* **454**, 145–201.

GRIGGS, A. J., ZINCHENKO, A. Z. & DAVIS, R. H. 2008 Gravity-driven motion of a drop or bubble near an inclined plane at low Reynolds number. *Intl J. Multiphase Flow* **34**, 408–418.

HOCKING, L. M. 1973 The effect of slip on the motion of a sphere close to a wall and of two adjacent spheres. *J. Engng Math* **7**, 207–221.

HUPPERT, H. E. 1982 Flow and instability of a viscous current down a slope. *Nature* **300**, 427–429.

JIAO, Y., GORB, S. & SCHERGE, M. 2000 Adhesion measured on the attachment pads of *Tettigonia viridissima* (orthoptera, insecta). *J. Exp. Biol.* **203**, 1887–1895.

JONES, A. F. & WILSON, S. D. R. 1978 The film drainage problem in droplet coalescence. *J. Fluid Mech.* **87**, 263–288.

MUSKHELISHVILI, N. I. 1963 *Some Basic Problems of the Mathematical Theory of Elasticity*. (trans. J. R. M. Radok). P. Noordhoff.

PEARSON, J. R. A. 1960 The instability of uniform viscous flow under rollers and spreaders. *J. Fluid Mech.* **7**, 481–500.

PETZOLD, L. R. 1983 A description of DASSL – a differential algebraic solver. In *Scientific Computing* (ed. R. S. Stepleman), pp. 65–68. North-Holland.

PINKUS, O. & STERNLICHT, B. 1961 *Theory of Hydrodynamic Lubrication*. McGraw-Hill.

SAFFMAN, P. G. & TAYLOR, G. I. 1958 The penetration of a fluid into a porous medium or Hele-Shaw cell containing a more viscous liquid. *Proc. R. Soc. Lond.* A **245**, 312–329.

SERAYSSOL, J.-M. & DAVIS, R. H. 1986 The influence of surface interactions on the elastohydrodynamic collision of spheres. *J. Colloid Interface Sci.* **114**, 54–66.

SKOTHEIM, J. M. & MAHADEVAN, L. 2005 Soft lubrication: the elastohydrodynamics of nonconforming and conforming contacts. *Phys. Fluids* **17**, 092101.

VERNEUIL, E., CLAIN, J., BUGUIN, A. & BROCHARD-WYART, F. 2003 Formation of adhesive contacts: spreading versus dewetting. *Eur. Phys. J.* E **10**, 345–353.

WARNER, M. R. E., CRASTER, R. V. & MATAR, O. K. 2004 Fingering phenomena associated with insoluble surfactant spreading on thin liquid films. *J. Fluid Mech.* **510**, 169–200.

WEEKLEY, S. J., WATERS, S. L. & JENSEN, O. E. 2006 Transient elastohydrodynamic drag on a particle moving near a deformable wall. *Quart. J. Mech. Appl. Math.* **59**, 277–300.